Monolithic perovskite/organic tandem solar cells with 23.6% efficiency enabled by reduced voltage losses and optimized interconnecting layer

Wei Chen[1,2,3,4,8], Yudong Zhu[2,6,8], Jingwei Xiu[2], Guocong Chen[2], Haoming Liang[3,4], Shunchang Liu[3,4], Hansong Xue[4], Erik Birgersson[4,7], Jian Wei Ho[4], Xinshun Qin[1], Jingyang Lin[5], Ruijie Ma[6], Tao Liu[6], Yanling He[5], Alan Man-Ching Ng[5], Xugang Guo[2], Zhubing He[2*], He Yan[6], Aleksandra B. Djurišić[1*] and Yi Hou[3,4*]

[1] Department of Physics, The University of Hong Kong, Pokfulam, Hong Kong SAR.

[2] Department of Materials Science and Engineering, Southern University of Science and Technology, No. 1088, Xueyuan Rd., Shenzhen, 518055, Guangdong, PR China.

[3] Department of Chemical and Biomolecular Engineering, National University of Singapore, 4 Engineering Drive 4, 117585 Singapore

[4] Solar Energy Research Institute of Singapore (SERIS), National University of Singapore, 7 Engineering Drive 1, 117574, Singapore.

[5] Department of Physics, Southern University of Science and Technology, No. 1088, Xueyuan Rd., Shenzhen, 518055, Guangdong, PR China.

[6] Department of Chemistry, The Hong Kong University of Science and Technology, Clear Water Bay, Kowloon, Hong Kong SAR.

[7] Department of Mechanical Engineering, National University of Singapore, 9 Engineering Drive 1, Singapore 117575, Singapore

[8] These authors contributed to this work equally.

[*]Correspondence to: hezb@sustech.edu.cn (Z.H.); dalek@hku.hk (A.D.) yi.hou@nus.edu.sg (Y.H.)

Abstract: Owing to the large chemical composition and bandgap tunability of both perovskite and organic semiconductors, perovskite/organic tandem solar cells are attractive for next-generation thin-film photovoltaics. However, their efficiency is limited by the open-circuit voltage loss of wide-bandgap perovskite subcells and the non-ideal interconnecting layers. Here, we report that the passivation of nickel oxide hole-transporting layers with benzylphosphonic acid leads to the suppression of interfacial recombination, boosting the voltage up to 1.26 V in a 1.79 eV-bandgap perovskite subcell. Then, we develop an optimized interconnecting layer structure based on a four-nm-thick sputtered indium zinc oxide layer inserted between organic bathocuproine and molybdenum oxide with enhanced electrical properties and transmittance in the near-infrared region. Through these improvements, we achieve a maximum efficiency of 23.60% (22.95% certified) in the perovskite/organic tandem solar cell. In addition, the tandem device retained 90% initial efficiency after 500-h maximum power point tracking under continuous one-sun illumination.

The potential of exceeding the Shockley–Quisser limit has stimulated intense interest in developing tandem solar cells (TSCs).[1-4] Perovskite materials have broad bandgap tunability (~1.17 eV–3.10 eV), which makes them an ideal choice as both front and bottom subcells in a TSC.[2,5,6] Perovskite/Si TSCs have achieved the highest power conversion efficiency (PCE) of 29.5% among perovskite-based TSCs,[7,8] which mainly targets utility application. Meanwhile, thin-film based tandems (e.g. perovskite/perovskite TSCs, perovskite/copper indium gallium selenide (CIGS) and perovskite/organic thin-film TSCs) have great potential for high-throughput and cost-effective production of flexible and lightweight TSCs and thus are promising for urban-integrated photovoltaic applications.[9]

Perovskite/organic TSCs have received increasing interest due to the recent improvement in the performance of organic photovoltaics (OPV) with the extension of spectral response beyond 1000 nm using narrow bandgap non-fullerene acceptors.[10-13] Perovskite/organic TSCs have the advantage of using orthogonal solvents for the perovskite and organic absorbers, potentially reducing the large-area solution-processing challenges related to perovskite/perovskite TSCs.[14] Compared to other bottom cell absorbers, organic materials have a larger chemical space and broader bandgap tunability, offering more bottom absorber options for perovskite-based TSCs.[10,15] However, the performance of perovskite/organic TSCs[16] still lags behind that of their thin-film tandem counterparts, such as perovskite/perovskite[17] and perovskite/CIGS[18] tandems.

There are two main reasons for the low efficiency of perovskite/organic TSCs. First, there are notable open circuit voltage (V_{oc}) losses in wide-bandgap (WBG) perovskite top cells. These are mainly attributable to surface recombination at the perovskite-charge transport layer interfaces and phase segregation under illumination. Although various approaches, including interfacial passivation, composition optimisation, and surface treatments, have been reported to boost the V_{oc} of 1.65–1.68 eV perovskite subcells,[19,20] it is still challenging to suppress the V_{oc} loss in 1.80 eV WBG perovskites.

Another reason is the optical and electrical losses in the interconnecting layer (ICL). An ideal ICL must be chemically inert, electrically conductive, and optically transparent[21,22] and provide enough recombination sites between the front and bottom subcells. In state-of-the-art perovskite/perovskite TSCs, the ICLs are commonly composed of ALD SnO_x and evaporated thin metals or thick (typically 10-100 nm) conductive transparent oxides (TCOs).[23-27] The ALD metal oxides and/or thick TCOs are critical for protecting the front perovskite cell from solvent damage in subsequent processing of bottom perovskites.[27-29] In contrast, perovskite/organic TSCs typically use evaporated thin metals in combination with organic/inorganic charge transport layers as ICLs.[16,17,30-35] However, the thin metal layer-based ICLs likely result in a large optical loss,[36,37] which limits the short circuit current density (J_{sc}) of the bottom cell and the efficiencies of TSCs. Thus, the optimisation of the design of a ICL to maintain efficient recombination while minimising optical losses remains a major challenge in fabricating perovskite/organic TSCs.

Here, we simultaneously reduced the V_{oc} loss in WBG perovskite subcells and optical and electrical losses of ICLs in perovskite/organic TSCs. By passivating the NiO_x hole transport layer (HTL) surface with benzylphosphonic acid (BPA), we reduced the surface recombination losses and achieved a maximum PCE over 17% with a V_{oc} of 1.26 V in a 1.79-eV bandgap perovskite. We further demonstrated a high-performance ICL consisting of a sputtered 4-nm-thick indium zinc oxide (IZO) layer sandwiched between a bathocuproine (BCP) layer and a molybdenum oxide (MoO_x) layer, resulting in a dramatic performance improvement compared to the ICL using 'BCP/Ag/MoO_x'. IZO-based ICLs show excellent near-infrared (NIR) transmittance, which minimises the current losses of the organic bottom

subcells. Moreover, the very thin IZO shows optimized surface coverage providing more recombination sites, which further allow effective charge recombination. The ICLs enable perovskite/organic TSCs with a V_{oc} of 2.06 V, a J_{sc} of 14.87 mA/cm^2 and an efficiency of 23.60% (22.95% certified) for small-area devices (0.08 cm^2) and 21.77% for large-area devices (1.05 cm^2). This performance surpassed that of previous perovskite/organic TSCs and approach the record performances of perovskite/perovskite and perovskite/CIGS TSCs. These tandem devices also maintained 90% initial efficiency after 500-h maximum power point tracking under continuous one-sun illumination.

Reduced V_{oc} loss of WBG perovskite by surface passivation

We first used a surface passivation strategy to reduce the V_{oc} losses of WBG perovskite front subcells. The surface chemistry of nickel oxide (NiO_x) is complex. The surface defects, e.g. different oxidation states of Ni, the presence of hydrates and other secondary phases act as surface recombination centres, affecting both efficiency and stability of the device.[38] Among different possible passivating molecules, those containing phosphonic acid are particularly interesting since they can have a variety of binding configurations (mono-, bi- and tri-dentate bonding thanks to hydroxyl and phosphoryl groups).[39] Here we employed benzylphosphonic acid (BPA) as the passivation molecule for the *p-i-n* WBG perovskite subcells (**Fig. 1a**). Previous reports have shown that the ideal bandgap of perovskite subcells is around 1.80 eV for perovskite/organic TSCs.[16,34] We therefore selected and fabricated 1.79 eV-bandgap perovskite, with a composition of $Cs_{0.25}FA_{0.75}Pb(I_{0.6}Br_{0.4})_3$, as the top subcells (see Method). From the absorption spectra (**Supplementary Fig. 1**), we observe that identical bandgaps (1.79 eV) were obtained for perovskite films deposited on NiO_x with and without BPA passivation. Contact angle measurement shows a reduced wettability of the BPA passivated substrate to polar solvents (**Supplementary Fig. 2a and 2b).** Scanning electron microscopy (SEM) and atomic force microscopy (AFM) characteristics suggested that the NiO_x surface passivation results in a smoother and more compact perovskite surface (**Supplementary Fig. 2c-2f**). The suppressed crystalline PbI_2 was also observed from X-ray diffraction (XRD) (**Supplementary Fig. 2g**), which is in line with previous reports of growing perovskites on reduced wettability substrates.[40-42] The cross-sectional scanning transmission electron microscopy (STEM) and energy dispersive X-ray (EDX) mapping of the BPA-passivated device show defined sharp interfaces, indicating the detailed thickness of each layer in the ICLs (**Supplementary Fig. 3**). X-ray photoelectron spectroscopy (XPS) also suggested that phosphonic acid is strongly bonded to the NiO_x surface (**Supplementary Fig. 4**).

BPA passivation effectively increases the PCE of single-junction devices (**Supplementary Fig. 5a**)**.** The maximum performance with BPA passivation is a PCE of 17.80% with a V_{oc} of 1.26 V, a J_{sc} of 17.90 mA/cm^2 and a FF of 78.9% under reverse *J-V* scans (see Methods), with a negligible hysteresis effect (**Fig. 1b and Table 1**). The steady power output (SPO) at maximum power point bias and the external quantum efficiency (EQE) spectra are consistent with the results from *J-V* scans under the speed of 274 mV/sec (**Supplementary Fig. 5b-c**). When compared with previous studies, this BPA passivation strategy yielded the highest V_{oc} for the 1.79-eV bandgap perovskites (**Fig. 1e and Supplementary Table 1).** To verify the accuracy of this result, these devices were certified at an authorised institute—SIMIT. The certified results are consistent with the results obtained in the lab (**Supplementary Fig. 6**).

To examine the effects of BPA interfacial passivation, we performed photoluminescence (PL) (**Supplementary Fig. 7a)** and time-resolved photoluminescence (TRPL) measurements (**Fig. 1c** and **Supplementary Table 2).** The PL results indicate that BPA passivation leads to a reduction in nonradiative interfacial recombination and, consequently, explains the observed increase in the V_{oc}, consistent with previous reports of effective defect passivation using self-assembled monolayers as HTLs.[18,43,44] The BPA passivation also improved the electroluminescence (EL) and EQE_{EL} of the WBG perovskite devices (**Supplementary Fig. 7b-c)**. The EQE_{EL} of the BPA passivated NiO_x device reached ~1.6 % at one-sun equivalent current injection, consistent with the enhanced EL intensity, which suggests the effective passivation effect of BPA. In addition, the increase in the work function (W_F) determined by photoelectron spectroscopy (UPS) (**Supplementary Fig. 8**) after BPA passivation allows better band alignment with the perovskite and thus more efficient charge collection. Moreover, based on both the *I-V* curves determined for hole-only devices (**Supplementary Fig. 9**) and Mott–Schottky plots (**Fig. 1d** and **Supplementary Note 1)**, a reduction in the trap densities was observed along with high built-in potential for the passivated devices, consistent with the improved V_{oc}. The passivation also resulted in improved shelf-life stability and operational stability (**Supplementary Fig. 10**) and improved stability under illumination for the perovskite films deposited on BPA-modified HTL (**Supplementary Fig. 11**), which is ascribed to the reduced interfacial trap density.[45]

ICL design for perovskite/organic tandem solar cells

Having demonstrated improved performance of the WBG perovskite subcell, we then considered the overall design of the perovskite/organic TSC. We selected the PM6 (also known as PBDB-T-2F):Y6 bulk heterojunction with the $P_{71}CBM$ ternary system as the absorber layer of the organic bottom subcell. This ternary system is based on a narrow bandgap of 1.36 eV[11], which is a good tandem bottom cell partner for a 1.79-eV bandgap perovskite front cell.[12] The detailed chemical structures of the organics and the absorption spectra of the bulk heterojunction layer are shown in **Supplementary Fig. 12**. We applied MoO_x as the HTL for OPV, and after device optimisation a PCE of 16.75% with a high J_{sc} of 26.80 mA/cm^2 was achieved (**Supplementary Fig. 13**).

Fig. 2a shows the architecture of the perovskite/organic TSC, where the C_{60}/BCP/carrier recombination layer (CRL)/MoO_x is the ICL. There are several CRLs reported in the literature for perovskite/organic TSCs. One commonly used CRL is thermally evaporated thin metal (1 nm Ag or Au).[14,16,31,34] Another possible alternative is a transparent conductive oxide (TCO) layer, e.g. indium zinc oxide (IZO) or ITO (10–100 nm), which have been used as CRLs in perovskite-based TSCs.[21] To examine these different CRLs in perovskite/organic TSCs, we integrated them into a tandem device and compared their performances (**Supplementary Fig. 14)**. **Fig. 2b** clearly shows the TSCs without any CRL exhibited the lowest performance with an S-shape curve due to the Schottky barrier between BCP and MoO_x, which hinder charge transport and consequently result in inefficient recombination. TSCs based on a 100-nm IZO CRL suffer from high leakage current, and also show low performances. While TSCs with 1-nm Ag CRL demonstrated a reasonable PCE of 18.59%, which is comparable to the previously reported perovskite/organic TSCs (**Fig. 2b and Supplementary Table 3**).[16,34] As we further reduced the IZO thickness down to 20 nm, the FF and V_{oc} increase accordingly, but it cannot catch up to the performance of the device using 1-nm Ag ICL. Ideally, ICL needs to exhibit maximum 'vertical conductivity' (maximum carrier recombination), maximum 'horizontal resistance' (minimum the current leakage) and high NIR transmittance, which will combine high J_{sc}, V_{oc} and FF in one device (**Supplementary Fig. 15a**). The 'horizontal resistances' (sheet resistance) of both 20-nm and

100-nm thick IZO layers are much smaller than that of the 1-nm Ag (**Supplementary Fig. 15b**), causing higher leakage current and low FF.

Among these four commonly used ICLs, we found that the 1-nm Ag ICL has the lowest NIR transmittance (**Fig. 2c).** This optical loss further increases the current losses of the organic bottom cells and leads to the current mismatch in the perovskite/organic TSCs. According to these results, we summarised the advantages and disadvantages of these four ICLs (**Supplementary Table 4**) and unfortunately there was no ICL that combines excellent optical and electrical properties.

Optical and electrical properties of thin IZO-based ICLs

If the IZO thickness is reduced to a few nanometres, in principle the IZO-based ICL will combine the desired charge transport in both the vertical and horizontal directions. To investigate the impact of thickness on the performance of TSCs, we deposited thin IZO layers with a thickness variation from 2 nm to 6 nm. From the top view images of BCP, 4-nm IZO and 1-nm Ag (**Supplementary Fig. 16**), we can clearly see the sputtered 4-nm IZO on BCP shows large and homogeneous grains (~30–50 nm), enabling a large surface coverage of ~96.2% on BCP (**Fig. 3a**). In contrast, the 1-nm Ag shows many 'islands' like clusters with a relatively low surface coverage of ~53.7% (**Fig. 3b**). Higher surface coverages in IZO ICLs contribute more recombination sites, shorter recombination lifetime, and thus more effective recombination. This is also in line with the *J-V* simulation results, in which the compact IZO thin film with high coverage exhibited a shorter recombination lifetime ($1x10^{-10}$s) than Ag clusters ($2x10^{-9}$s), and a better efficiency (**Supplementary Fig. 17**).

As shown in **Fig. 3c,** the 4-nm IZO-based ICLs exhibited much higher NIR transmittance than that of 1 nm Ag-based ICLs. We further employed STEM and EDX mapping to examine in detail the perovskite/organic TSCs with 4-nm IZO-based ICLs. The sharp interfaces within the layer stacks can be observed in the STEM image of the tandem cell (**Supplementary Fig. 18**). EDX mapping of the tandem cell (**Supplementary Fig. 19a**) further confirmed each key element distribution. Furthermore, the high-resolution STEM and EDX mapping (**Fig. 3d** and **Supplementary Fig. 19b**) of the enlarged ICL region clearly showed a thin layer of IZO sandwiched between C_{60}/BCP and MoO_x layers.

Fig. 3e shows the *J-V* characteristics of the perovskite/organic TSCs with the IZO thickness from 2 nm to 6 nm. The corresponding parameters are shown in **Supplementary Table 5** and summarised in **Supplementary Fig. 20**. There were noticeable S-shaped *J-V* curves for the TSCs with an IZO thickness below 4 nm, which is mainly attributed to the inefficient carrier recombination in the ICLs. When the thickness is increased to 4 nm, the S-shaped *J-V* curve disappeared. However, when IZO thickness is further increased to 6 nm, it starts to show a higher current leakage and reduced FF.

To further explore the working mechanism of IZO ICLs, we measured the Hall effect of the IZOs with varied thicknesses (**Supplementary Fig. 21**). It was found that balanced vertical and horizontal transport appears at around 4 nm. The thicker, and thinner, IZOs lead to low shunt resistance, and high series resistance, respectively. The *J-V* characteristics of the diode devices further determine the vertical electrical conductivity of 4-nm IZO is slightly higher than that of 1-nm Ag (**Fig. 3f)**.

We also performed a UPS measurement to determine the band alignment at the BCP/IZO/MoO_x interfaces (**Supplementary Fig. 22a-c**). The detailed energy diagrams after the Fermi level alignment are depicted in **Supplementary Fig. 22d**. We can see a strong

band bending at the BCP/MoO_x interfaces due to the large work function differences. This is likely to cause a large Schottky barrier at these interfaces, leading to inefficient recombination within the ICL and consequently large S-shaped *J-V* curves of the tandem devices without any CRL. Inserting 4-nm IZO upshifts the energy level of BCP and dramatically reduces the barrier, allowing a quasi-ohmic contact between BCP and MoO_x, resulting in barrier-free transport of electrons from the WBG perovskite front subcells into the IZO recombination centres, where holes and electrons are effectively recombined.[21]

Fig. 3g shows a comparison of the *J-V* curves of the TSCs with IZO and Ag-based ICLs. Replacing Ag with thin IZO, the tandem devices showed a clear performance improvement from 19.50% to 22.90% (**Supplementary Table 6**). This is largely driven by the enhancement of J_{sc}. EQE measurements highlight the advantage of switching from a thin metal-based ICL to a thin IZO-based ICL. The reduction of optical and consequent current loss in the 700- to 900-nm range, resulted in a clear J_{sc} increase of 1.46 mA/cm^2 (**Fig. 3h**). The performance statistics of perovskite/organic TSCs with IZOs and Ag-based ICLs confirmed the advantages of the 4-nm IZO (**Supplementary Fig. 23**).

Optimal performance of perovskite/organic tandem devices

Fig. 4a presents the *J–V* curves of the champion perovskite/organic TSCs with 4-nm IZO-based ICLs. The corresponding photovoltaic parameters are summarised in **Table 2**. Our best small-area tandem device yielded a PCE of 23.60% from *J-V* scan, with a V_{oc} of 2.06 V, a J_{sc} of 14.83 mA/cm^2 and FF of 77.2% under reverse scan with almost no hysteresis. The device with IZO-based ICLs exhibited a stabilised SPO of 23.54% (**Supplementary Fig. 24**) and excellent current matching between the two subcells, as estimated from the integrated EQE (**Fig. 4b**). As summarised in **Supplementary Table 7**, our champion tandem cell showed a significant performance improvement compared to the previous studies.[14,16,46] To confirm the reliability of our results, we also sent the tandem devices to the authorised institute SIMIT for certification, and a certified PCE of 22.94% was obtained under reverse scan, which aligns well with the values we measured in our lab (**Supplementary Fig. 25**). We also prepared perovskite/organic TSCs with a large area of 1.05 cm^2, as shown in **Fig. 4c**. The champion device exhibited a PCE of 21.77%, with a similar V_{oc} of 2.06 V but a slightly decreased J_{sc} and FF compared to the small-area device (**Table 2**). The device also showed a high stabilised power output of 21.58% and excellent current matching between the two subcells, as estimated from the EQE measurements (**Supplementary Fig. 26**).

We evaluated the stability of the tandem devices with different ICLs. The TSCs with IZO ICLs exhibited improved shelf-life compared to devices with Ag ICLs when stored in the dark in an N_2-filled glovebox, as shown in **Supplementary Fig. 27**. This is likely attributable to the thicker and more compact IZO layer, which provides better protection of the perovskite layer than the Ag clusters.[47] More importantly, the IZO layers are more chemically stable than the Ag ones, as the metals are prone to react with the halide ions in the perovskite.[48,49]

We also compared the thermal stability of the two TCSs under different aging temperatures and found that the TSCs experienced a relatively faster degradation at 85 ^oC but were relatively stable at 65 ^oC, which might be caused by the unstable MoO_x (**Supplementary Fig. 28**).[50] We further evaluated the MPP stability of the TSCs with IZO ICLs, as shown in **Fig. 4d.** After a fast burn-in loss, the TSC was stabilised and retained ~90% of its initial efficiency after 500 h. The initial burn-in degradation was likely due to the

change of bulk-heterojunction morphology and the fast ion movements at the perovskite and organic interfaces.[51]

Conclusions

We demonstrated that the surface passivation of NiO_x using BPA results in suppression of interfacial defects, which boosts the V_{oc} and PCE of WBG perovskite solar cells. We also developed a sputtered 4-nm-thick IZO ICL that confers both excellent electrical and optical properties. These combined enhancements enabled a maximum PCE of 23.60% (22.94% certified) in perovskite/organic TSCs. Our approach demonstrates the effectiveness of the strategy of simultaneously reducing optical losses (by avoiding metal in ICLs) and V_{oc} loss in WBG perovskite devices (by interfacial defect passivation). We experimentally and theoretically unveil the interplay of ICL surface coverage, lateral (vertical) transport, and recombination lifetime, which provides an important design guideline for ICLs in perovskite-based TSCs. This work shows the great potential of perovskite/organic TSCs for catching up or even surpassing the performances of perovskite/perovskite TSCs and perovskite/CIGS TSCs. These findings will reduce the efficiency-stability-flexibility gap of perovskite solar cells in the future. Developing novel narrow bandgap organics, highly stable HTLs, and suppressing phase segregation in wide-bandgap perovskite will likely be essential for the future of perovskite/organic TSCs.

Methods

Materials. Anhydrous solvents including N,N-dimethylformamide (DMF), dimethyl sulfoxide (DMSO), methyl acetate (MeAc), and materials including nickel(II) nitrate hexahydrate (99.999 %), benzylphosphonic acid (BPA, 97%), cesium iodide (CsI, 99.999%) were purchased from Sigma-Aldrich. Cesium bromide (CsBr, 99.999%) was purchased from Alfa Aesar. Lead (II) iodide (PbI_2) (Product number: L0279) and lead (II) bromide ($PbBr_2$) (Product number: L0288) were purchased from TCI. Formamidinium bromide (FABr), formamidinium iodide (FAI) and phenethylammonium iodide (PEAI) were purchased from GreatCell Solar Ltd. $PC_{71}BM$, C_{60} and BCP were obtained from Daeyeon Chemicals Co., Ltd. PM6, Y6 and PNDIT-F3N were obtained from Solarmer Materials Inc. All materials above were used as received.

Synthesis of NiO_x nanoparticles. The NiO_x particles were prepared in lab, which is based on our previous recipe.[52] Firstly, the nickel (II) nitrate hexahydrate (9 g) were fully dissolved in 120 ml DI water, in which 120 ml sodium hydroxide (1 mol/ml) were added using dropping funnel (2-3 drop/second) under vigorous stirring at room temperature. The solution were stirred for another 5 min to complete the reaction, then green raw products ($Ni(OH)_2$) were collected by centrifugation at 6000 rpm for 8 mins, followed by thorough washing with DI water. Above centrifugation and washing steps were repeated at least three times until the pH values of the supernatants were neutral. Then, the obtained raw products were thoroughly dried with freeze-drying equipment for at least 48 h. By using the freeze-drying, it is expected to obtain high quality NiO_x nanoparticles with better crystallinity and smaller particle sizes than the thermal drying recipe. Finally, the powders were sintered at 275 -280 ^oC for 2 h with tube furnace instead of muffle one (ramping up rate: 2-3 ^oC/min; ramping down rate: 5 ^oC/min). Both freeze-drying and annealing in a tube furnace are critical steps in obtaining high quality NiO_x.

1.79 eV WBG perovskite front cells. The precursor solution was prepared by mixing FAI, FABr, CsI, CsBr, $PbBr_2$ and PbI_2 in DMF/DMSO (4/1) with 1 M concentration. The molar

ratio of FA^+/Cs^+ and I^-/Br^- are kept at 75/25 and 6/4, respectively. 1 mol% excess of PbI_2 is found beneficial for device performance. The precursor solution was stirred at 60 ^oC for 24 hrs. After cooling to room temperature. The devices with *p-i-n* structure were fabricated following a configuration of ITO/NiO_x/BPA/perovskite/C_{60}/BCP/Ag. ITO glass was cleaned by sequentially washing with detergent, deionized water, acetone, and isopropanol. The substrates were dried with N_2 and cleaned by UV ozone for 15 min. The homemade NiO_x nanoparticles ink (20 mg/ml in DI water) were spin coated on the clean ITO substrates as hole transporting layers. After annealing for 15 min at 110 ^oC, NiO_x coated ITO substrates were then transferred to N_2 glovebox and the NiO_x films were treated with BPA (1 mg/ml in anhydrous IPA) by spin-coating at 6000 rpm for 30s, and then annealing at 100 ^oC for 10 min. Avoid exposure to air when weighting the BPA powders and preparing solution. The BPA solution (150 μL) was loaded on NiO_x, and waiting time before spin-coating was 10 s. The perovskite films were spin coated on HTLs substrates at 6000 rpm with accelerating speed of 5000 for 35s, during spin coating, methyl acetate (200 μL) was slowly dropped at 15 s before ending. The films were then annealed at 100 ^oC for 15 min. After cooling down to room temperature, 100 μl PEAI solution (1 mg/ml in IPA) was quickly dropped on the perovskite and spin coated with 4000 rpm for 30 s and annealed at 100 ^oC for 10 min.[53] The substrates were then transferred into high vacuum thermal evaporator where the ETLs C_{60} (25 nm), BCP (12 nm) and metal electrode (Ag (120 nm) were subsequently evaporated. The active area was defined with a shadow mask.

Deposition of IZO layer. IZO films were deposited on substrates by RF sputtering technique (Dual Chamber Deposition, KYKY-500CK-500ZF).[54] The 4 inch target material, 80% In_2O_3 and 20% ZnO were used. Pure Argon is used as a process gas. The base pressure was kept 1.88×10^{-7} Torr before the deposition to eliminate the contribution of the water during the processing. The deposition rate of the optimized IZO films was 20 Å/min at room temperature without any intentional heating. The work pressure was kept at 4-2.5 $\times10^{-3}$ Torr. The sputtering power is fixed to 50 W. The distance between sample holder and target is ~10 cm.

Perovskite/organic tandem solar cells. After deposition of C_{60} and BCP, the WBG perovskite subcells were transferred to sputter system, where the 4 nm IZO were sputtered on top as recombination layer, then 25 nm MoO_x was thermally evaporated as an HTL for the organic subcells. The ternary organic solutions were prepared by weighting PM6, Y6 and $PC_{71}BM$ with weight ratio of 1:1.2:0.2, and dissolving in chloroform with concentration of 8 mg/ml (referring to PM6) and with 0.5% 1-CN additive.[11] Organic solution was stirred at 50 ^oC for 1.5 hrs. Organic films were deposited by drop cast at 3000 rpm for 45 s, and annealed at 90 ^oC for 5 min. After cooling down, PNDIT-F3N (0.5 mg/ml in methanol) was drop cast on top as a n-type interfacial layer.[55] Finally 120 nm Ag was thermal evaporated as top electrode with metal shadow mask. The device area is 14.25 mm^2.

Solar cell characterization. *J-V* measurements were carried out using a Keithley 2400 sourcemeter in ambient environment at ~23 ºC and ~45% RH. The devices were measured both in reverse scan and forward scan with 10 mV interval and 10 ms delay time. The steady state power output (SPO) curves were recorded by tracing the current density at bias (voltage at maximum power point) for at least 5 min after J-V measurements. Illumination was provided by an Oriel Sol3A solar simulator with AM1.5G spectrum and light intensity of 100 mW/cm^2, which was calibrated by a standard Si diode (a KG-5 reference cell was used for the measurements of WBG perovskite solar subcells). For perovskite/organic tandem solar cells, the solar simulator spectrum was finely tuned to ensure that spectral mismatch was within 3% for both subcells. During *J-V* measurement, optical aperture mask (8 mm^2) was used to verify the accurate cell area. EQE measurements for devices were conducted with an

Enli-Tech (Taiwan) EQE measurement system. For EQE measurement of tandem cells, the WBG perovskite front subcells were measured while saturating the organic bottom subcells with continuous light from a halogen lamp with an 800 nm polarized optical filter, while the organic bottom subcells were measured while saturating the perovskite front subcells with continuous light from a halogen lamp with 500 nm polarized optical filter. The power for halogen lamp is ~250 W. No bias voltage was applied for the EQE measurement of both subcells.

Device stability. For shelf-life and thermal stability measurements, the devices without encapsulation were kept room temperature or corresponding temperature under dark except during the *J-V* measurement, and the *J-V* curves were recorded in certain time intervals. For the maximum power point (MPP) tracking tests under illumination, the device was fixed at the V_{mpp} and the current density variation under ambient environment (~23.5 ^{o}C, ~34% RH) was recorded without controlling the device temperature. The devices were carefully encapsulated with desiccant coverage in the cell area and epoxy edge sealing following our previous encapsulation recipe.[56]

SEM, STEM and EDX mapping. Top-view morphology was analyzed by TESCAN MIRA3. A FEI Helios Nanolab 600i dual beam focus ion beam/field emission gun-scanning electron microscope (FIB/FEGSEM) was used to prepare cross-section for STEM imaging and analysis. FEI Talos transmission electron microscope (TEM) with Super-X EDX was employed to acquire the STEM-EDX data with STEM-HAADF (high-angle annular dark field) mode.

Theoretical stimulation. In modelling the *J-V* characteristics of the perovskite/organic tandem solar cell, the three-dimensional structure of the tandem device is reduced into a one-dimensional model in the x-direction, under the condition that optical field, electron and hole fluxes in the y- and z- direction are negligible (main parameters used in our modelling were tabulated below.). The optical absorptions in both perovskite and organic layers are calculated in MATLAB with transfer matrix method.[57] The optical generation profiles are then imported into COMSOL Multiphysics to be coupled with the drift-diffusion equations for perovskite top-cell,[58] and organic bottom-cell[59] in solving the transport of the charge carriers as well as the potential within the tandem device. Trap-assisted recombination mechanism is implemented to model the recombination junction in the device.[60] Its recombination coefficient is calibrated with the experiment J-V curve of the tandem device through a non-linear curve-fitting algorithm in the least-square manner in MATLAB. Here, the direct solver MUMPs is selected as the nonlinear solver with a relative convergence tolerance of 10^{-3}. The fluxes of the charge carriers are calculated with Lagrange multipliers with weak constraints for evaluating the output current. All the computational domains are solved with a mesh size of 1 nm while the boundaries with size of 0.1 nm.

Other characteristics. The X-ray diffraction patterns were obtained using a BRUKER ECO D8 series. Absorption and transmittance spectra were measured with LAMBDA 750 UV/Vis/NIR spectrophotometer. PL and time resolved PL spectra were measured using a Spectrofluorometer (FS5, Edinburgh instruments) and 405 nm pulsed laser was used as excitation source for the measurement. Sheet resistances for IZO films were measured with Keithley 4200A-SCS. UPS measurements were performed on an ESCALAB 250Xi, Thermo Fisher (by using Al Kα x-ray source) under high vacuum (10^{-9} mbar). Mott–Schottky characteristics were analyzed with a Zahner IM6e electrochemical station (Zahner, Germany) in ambient environment of 25 ºC and 38% RH.

Data availability. All data generated or analysed during this study are included in the published article and its Supplementary Information and Source Data files.

Acknowledgements

This work is supported by the National Natural Science Foundation of China (NSFC) (Nos. 61775091, U2001216), Science, Technology and Innovation Commission of Shenzhen Municipality (No. JCYJ20180504165851864) and the Shenzhen Key Laboratory Project (No. ZDSYS201602261933302) and Natural Science Foundation of Shenzhen Innovation Committee (Nos. JCYJ20150529152146471, JCYJ20170818141216288). A.B.D. would like to acknowledge support from RGC CRF grant C5037-18G and C7018-20G, Seed Funding for Strategic Interdisciplinary Research Scheme of the University of Hong Kong and Shenzhen Science and Technology Commission Projects No. JCYJ20170818141216288. Y.H. acknowledges the support from the National University of Singapore (NUS) Presidential Young Professorship (R-279-000-617-133 and R-279-001-617-133). This work was authored in part by SERIS, a research institute at the NUS. SERIS is supported by NUS, the National Research Foundation Singapore (NRF), the Energy Market Authority of Singapore (EMA) and the Singapore Economic Development Board (EDB). The authors thank the Materials Characterization and Preparation Center (MCPC) and the Pico Center of SUSTech for some characterizations in this work.

Author contributions

W.C., A.B.D. and Y.H. conceived the idea and designed the experiments. Y.H., A.B.D. and Z.H. supervised the project. Y.H., A.B.D., W.C., H.L., H.Y., A.M.N., X.G. and Z.H. composed and revised the paper. W.C. fabricated and characterized the perovskite and tandem solar cells., Y.Z., J.L. and S.L. helped perform the related device electrical characteristics and measurements. H.X. and E.B managed to perform the simulation and analyze the data. R.M. and T.L. helped to optimize the organic solar cells. Y.Z., J.X. and G.C. finished the FIB, STEM and HRTEM characteristics and the IZO sputtering. J.L. helped perform the optical measurement and Y.L.H. analyze the data. G.C. and J.X. performed the XPS, UPS, PL and EIS measurements and data analysis. Y.Z., J.H. and X.Q. helped perform other related characteristics and measurements. All authors discussed and analyzed the results.

Competing interests

The authors declare no competing interests.

Tables

Table 1. Summary of the optimal WBG perovskite solar cell performances using different HTLs.

Devices	***Scan direction***	V_{oc} **(V)**	J_{sc} **(mA/cm^2)**	***FF*** **(%)**	***PCE*** **(%)**
NiO_x	Reverse	1.18	17.12	76.9	15.53
	Forward	1.18	17.11	77.4	15.63
NiO_x/BPA	Reverse	1.26	17.90	78.9	17. 80
	Forward	1.25	17.94	78.4	17.59

Table 2. Performance comparison of the champion perovskite/organic TSCs with 4 nm IZO CRL under reverse and forward scan.

Champion devices	*Scan direction*	V_{oc} (V)	J_{sc} (mA/cm^2)	*FF* (%)	*PCE* (%)
4 nm IZO (0.08 cm^2)	reverse	2.063	14.83	77.2	23.60
	forward	2.061	14.84	77.1	23.57
4 nm IZO (1.05 cm^2)	reverse	2.062	14.24	74.4	21.77
	forward	2.059	14.23	74.1	21.72

Figure Legends/Captions (for main text figures)

Fig. 1. Suppression of V_{oc} loss of WBG perovskite solar cells using BPA passivation strategy. a) Schematic diagrams show the BPA passivation of NiO_x HTLs. The passivation can substantially suppress the surface defects/trap sites. The NiO_x HTL is denoted as the grey region. The blue, black, ashy, green and purple colors in the ball-and-stick models represent N, C, H, O and P atoms, respectively; b) *J-V* curves (forward and reverse scan) of the best WBG perovskite subcells with and without BPA passivation of NiO_x HTLs under AM 1.5G illumination (100 mW/cm^2); c) PL decay dynamics of the perovskite films deposited on NiO_x HTLs with and without BPA passivation; d) Mott-Schottky (M-S) plot analysis from capacitance-voltage measurements for WBG perovskite subcells at 10 kHz under dark condition. Linear fitting is used to calculate the built-in potentials; e) The evolution of the achieved V_{oc} and PCE as function of bandgap in the *p-i-n* WBG perovskite devices reported by previous literature (Ref. S(number) denotes references in the supplementary information. A more detailed summary can be found in Supplementary Table 1). The best efficiency obtained in this work is also shown for comparison. The S-Q limit (maximum theoretical value) is indicated for comparison.

Fig. 2. Design of interconnection layers in perovskite/organic tandem solar cells. a) Schematic diagram showing the *p-i-n* perovskite-organic tandem solar cells. The dashed grey frame boxes the interconnecting layers (ICLs) region, which functions as a series connect for the front and bottom subcells. CRL: Carrier recombination layer. The design of ICLs with four types of CRLs are depicted in the frame; b) *J-V* curves (reverse scan) of the perovskite-organic TSCs with different ICLs. The cells in each substrate were electrically isolated by mechanical scribing; c) Transmittance spectra of the perovskite subcells with four types of CRLs. The solid and dashed lines refer to transmittance and reflection, respectively, and the horizontal dashed black line serves as a guide for comparison.

Fig. 3. Characteristics and working mechanism of the perovskite/organic tandems with thin IZO-based ICLs. a-b) TEM image of the 4 nm IZO (a) and 1 nm Ag (b) on BCP which was thermally deposited on copper mesh with ultra-thin carbon films; c) Transmittance spectra of the perovskite subcells with 4 nm IZO and 1 nm Ag-based ICLs. The solid and dashed lines refer to transmittance and reflection, respectively, and the horizontal dashed black line serves as a guide for comparison; d) High-resolution STEM of the 4 nm IZO-based ICLs region in the TSCs, and the EDX mapping showing the elemental distribution of Zn, Mo, O; e) *J-V* curves (reverse scan) of the perovskite/organic TSCs using IZO-based ICLs

with different thickness; f) *J-V* characteristics of the diode devices with the structure of ITO/BCP/IZO(Ag)/MoO_x/Ag; g) *J-V* curves (reverse scan) of the perovskite/organic TSCs with IZO and Ag-based CRLs, note that the devices were from the same batch; h) External quantum efficiency (EQE) spectra of the TSCs with IZO and Ag-based ICLs. Reflection (denoted as 1-R) and sum (total EQE of individual subcells) curves are also presented. Dashed and solid light blue curves represent 1-R and sum for TSCs with Ag-based ICLs, and dashed and solid brown curves represent 1-R and sum for TSCs with IZO-based ICLs. The integrated J_{sc} of the organic bottom subcells with IZO-based ICLs demonstrate an improvement of 1.46 mA/cm^2 (shaded area) compared to the Ag-based ICLs.

Fig. 4. Optimal performance of the perovskite/organic tandems. a) *J-V* curves (reverse and forward scan) of the champion small area (0.08 cm^2) perovskite/organic TSC with IZO-based ICLs. For the champion device, the glass side of the substrate was coated with a 100 nm thick lithium fluoride as an antireflection layer; b) EQE and reflection (denoted as 1-R) spectra for the champion device. The front perovskite and bottom organic subcells exhibit integrated J_{sc} values of 14.32 and 14.37 mA/cm^2, respectively. The sum curve represents the total EQE of both front and rear subcells in the tandem; c) *J-V* curves (reverse and forward scan) of the champion large area perovskite/organic TSC with IZO-based ICLs with, inset shows a photograph of the large area tandem device; d) Operational stability evaluation of the encapsulated small area perovskite/organic TSC with IZO-based ICL using maximum power point (MPP) tracking method under N_2 environments and without temperature control.

References:

1 Anaya, M., Lozano, G., Calvo, M. E. & Míguez, H. ABX_3 Perovskites for Tandem Solar Cells. *Joule* **1**, 769-793 (2017).

2 Leijtens, T., Bush, K. A., Prasanna, R. & McGehee, M. D. Opportunities and challenges for tandem solar cells using metal halide perovskite semiconductors. *Nat. Energy* **3**, 828-838 (2018).

3 Bush, K. A. *et al.* 23.6%-efficient monolithic perovskite/silicon tandem solar cells with improved stability. *Nat. Energy* **2**, 17009 (2017).

4 Hou, Y. *et al.* Efficient tandem solar cells with solution-processed perovskite on textured crystalline silicon. *Science* **367**, 1135-1140 (2020).

5 Eperon, G. E. *et al.* Perovskite-perovskite tandem photovoltaics with optimized band gaps. *Science* **354**, 861-865 (2016).

6 McMeekin, D. P. *et al.* A mixed-cation lead mixed-halide perovskite absorber for tandem solar cells. *Science* **351**, 151-155 (2016).

7 *Best Research-Cell Efficiency Chart (NREL, accessed April 2021),* https://www.nrel.gov/pv/assets/pdfs/best-research-cell-efficiencies.20200104.pdf

8 Al-Ashouri, A. *et al.* Monolithic perovskite/silicon tandem solar cell with >29% efficiency by enhanced hole extraction. *Science* **370**, 1300-1309 (2020).

9 Li, H. & Zhang, W. Perovskite Tandem Solar Cells: From Fundamentals to Commercial Deployment. *Chem. Rev.* **120**, 9835-9950 (2020).

10 Yan, C. *et al.* Non-fullerene acceptors for organic solar cells. *Nat. Rev. Mater* **3**, 18003 (2018).

11 Yuan, J. *et al.* Single-Junction Organic Solar Cell with over 15% Efficiency Using Fused-Ring Acceptor with Electron-Deficient Core. *Joule* **3**, 1140-1151 (2019).

12 Zhang, M. *et al.* Single-layered organic photovoltaics with double cascading charge transport pathways: 18% efficiencies. *Nat. Commun.* **12**, 309 (2021).

13 Yao, H., Wang, J., Xu, Y., Zhang, S. & Hou, J. Recent Progress in Chlorinated Organic Photovoltaic Materials. *Accounts. Chem. Res.* **53**, 822-832 (2020).

14 Xie, Y. M. *et al.* Monolithic perovskite/organic tandem solar cells: Developments, prospects, and challenges. *Nano Select* **2**, 1266-1276 (2021).

15 Meng, L. *et al.* Organic and solution-processed tandem solar cells with 17.3% efficiency. *Science* **361**, 1094-1098 (2018).

16 Chen, X. *et al.* Efficient and Reproducible Monolithic Perovskite/Organic Tandem Solar Cells with Low-Loss Interconnecting Layers. *Joule* **4**, 1594-1606 (2020).

17 Lin, R. *et al.* Monolithic all-perovskite tandem solar cells with 24.8% efficiency exploiting comproportionation to suppress Sn(ii) oxidation in precursor ink. *Nat. Energy* **4**, 864-873 (2019).

18 Al-Ashouri, A. *et al.* Conformal monolayer contacts with lossless interfaces for perovskite single junction and monolithic tandem solar cells. *Energy Environ. Sci.* **12**, 3356-3369 (2019).

19 Peña-Camargo, F. *et al.* Halide Segregation versus Interfacial Recombination in Bromide-Rich Wide-Gap Perovskite Solar Cells. *ACS Energy Lett.* **5**, 2728-2736 (2020).

20 Mahesh, S. *et al.* Revealing the origin of voltage loss in mixed-halide perovskite solar cells. *Energy Environ. Sci.* **13**, 258-267 (2020).

21 Ko, Y., Park, H., Lee, C., Kang, Y. & Jun, Y. Recent Progress in Interconnection Layer for Hybrid Photovoltaic Tandems. *Adv. Mater.* **32**, e2002196 (2020).

22 De Bastiani, M. *et al.* Recombination junctions for efficient monolithic perovskite-based tandem solar cells: physical principles, properties, processing and prospects. *Mater. Horiz.* **7**, 2791-2809 (2020).

23 Zhao, D. *et al.* Low-bandgap mixed tin–lead iodide perovskite absorbers with long carrier lifetimes for all-perovskite tandem solar cells. *Nat. Energy* **2**, 17018 (2017).

24 Li, C. *et al.* Low-bandgap mixed tin–lead iodide perovskites with reduced methylammonium for simultaneous enhancement of solar cell efficiency and stability. *Nat. Energy* **5**, 768-776 (2020).

25 Yu, Z. *et al.* Simplified interconnection structure based on C60/SnO_{2-x} for all-perovskite tandem solar cells. *Nat. Energy* **5**, 657-665 (2020).

26 Yang, Z. *et al.* Enhancing electron diffusion length in narrow-bandgap perovskites for efficient monolithic perovskite tandem solar cells. *Nat. Commun.* **10**, 4498 (2019).

27 Palmstrom, A. F. *et al.* Enabling Flexible All-Perovskite Tandem Solar Cells. *Joule* **3**, 2193-2204 (2019).

28 Zhao, D. *et al.* Efficient two-terminal all-perovskite tandem solar cells enabled by high-quality low-bandgap absorber layers. *Nat. Energy* **3**, 1093-1100 (2018).

29 Eperon, G. E. *et al.* Perovskite-perovskite tandem photovoltaics with optimized band gaps. *Science* **354**, 861-865 (2016).

30 Xiao, K. *et al.* All-perovskite tandem solar cells with 24.2% certified efficiency and area over 1 cm^2 using surface-anchoring zwitterionic antioxidant. *Nat. Energy* **5**, 870-880 (2020).

31 Li, Z. *et al.* Hybrid Perovskite-Organic Flexible Tandem Solar Cell Enabling Highly Efficient Electrocatalysis Overall Water Splitting. *Adv. Energy Mater.* **10**, 2000361 (2020).

32 Lang, K. *et al.* High Performance Tandem Solar Cells with Inorganic Perovskite and Organic Conjugated Molecules to Realize Complementary Absorption. *J. Phys. Chem. Lett.* **11**, 9596-9604 (2020).

33 Chen, C.-C. *et al.* Perovskite/polymer monolithic hybrid tandem solar cells utilizing a low-temperature, full solution process. *Mater. Horiz.* **2**, 203-211 (2015).

34 Xie, S. *et al.* Efficient monolithic perovskite/organic tandem solar cells and their efficiency potential. *Nano Energy* **78**, 105238-105245 (2020).

35 Zeng, Q. *et al.* A two-terminal all-inorganic perovskite/organic tandem solar cell. *Sci. Bull.* **64**, 885-887 (2019).

36 Kim, S. & Lee, J.-L. Design of dielectric/metal/dielectric transparent electrodes for flexible electronics. *J. Photon. Energy* **2**, 021215-021211 (2012).

37 Axelevitch, A., Gorenstein, B. & Golan, G. Investigation of Optical Transmission in Thin Metal Films. *Phys. Procedia* **32**, 1-13 (2012).

38 Di Girolamo, D. *et al.* Progress, highlights and perspectives on NiO in perovskite photovoltaics. *Chem. Sci.* **11**, 7746-7759 (2020).

39 Ali, F., Roldán-Carmona, C., Sohail, M. & Nazeeruddin, M. K. Applications of Self-Assembled Monolayers for Perovskite Solar Cells Interface Engineering to Address Efficiency and Stability. *Adv. Energy Mater.* **10**, 2002989 (2020).

40 Bi, H. *et al.* Interfacial defect passivation and stress release by multifunctional KPF_6 modification for planar perovskite solar cells with enhanced efficiency and stability. *Chem. Eng. J.* **418**, 129375 (2021).

41 Zhang, J. *et al.* Obstructing interfacial reaction between NiO_x and perovskite to enable efficient and stable inverted perovskite solar cells. *Chem. Eng. J.* **426**, 131357 (2021).

42 Du, Y. *et al.* Polymeric Surface Modification of NiO_x-Based Inverted Planar Perovskite Solar Cells with Enhanced Performance. *ACS Sustain. Chem. Eng* **6**, 16806-16812 (2018).

43 Tress, W. Perovskite Solar Cells on the Way to Their Radiative Efficiency Limit - Insights Into a Success Story of High Open-Circuit Voltage and Low Recombination. *Adv. Energy Mater.* **7**, 1602358 (2017).

44 Wang, Q. *et al.* Effects of Self-Assembled Monolayer Modification of Nickel Oxide Nanoparticles Layer on the Performance and Application of Inverted Perovskite Solar Cells. *Chemsuschem* **10**, 3794-3803 (2017).

45 Chen, W. *et al.* Molecule-Doped Nickel Oxide: Verified Charge Transfer and Planar Inverted Mixed Cation Perovskite Solar Cell. *Adv. Mater.* **30**, 1800515 (2018).

46 Liu, L., Xiao, Z., Zuo, C. & Ding, L. Inorganic perovskite/organic tandem solar cells with efficiency over 20%. *J. Semicond.* **42**, 020501 (2021).

47 Zuo, L., Shi, X., Fu, W. & Jen, A. K. Highly Efficient Semitransparent Solar Cells with Selective Absorption and Tandem Architecture. *Adv. Mater.* **31**, e1901683 (2019).

48 Bush, K. A. *et al.* Thermal and Environmental Stability of Semi-Transparent Perovskite Solar Cells for Tandems Enabled by a Solution-Processed Nanoparticle Buffer Layer and Sputtered ITO Electrode. *Adv. Mater.* **28**, 3937-3943 (2016).

49 Fu, F. *et al.* High-efficiency inverted semi-transparent planar perovskite solar cells in substrate configuration. *Nat. Energy* **2**, 16190 (2016).

50 Schloemer, T. H. *et al.* The Molybdenum Oxide Interface Limits the High-Temperature Operational Stability of Unencapsulated Perovskite Solar Cells. *ACS Energy Lett.* **5**, 2349-2360 (2020).

51 Heumueller, T. *et al.* Disorder-Induced Open-Circuit Voltage Losses in Organic Solar Cells During Photoinduced Burn-In. *Adv. Energy Mater.* **5**, 1500111 (2015).

52 Chen, W., Xu, L., Feng, X., Jie, J. & He, Z. Metal Acetylacetonate Series in Interface Engineering for Full Low-Temperature-Processed, High-Performance, and Stable Planar Perovskite Solar Cells with Conversion Efficiency over 16% on 1 cm^2 Scale. *Adv. Mater.* **29**, 1603923 (2017).

53 Chen, C. *et al.* Arylammonium-Assisted Reduction of the Open-Circuit Voltage Deficit in Wide-Bandgap Perovskite Solar Cells: The Role of Suppressed Ion Migration. *ACS Energy Lett.* **5**, 2560-2568 (2020).

54 Ying, Z. *et al.* Sputtered Indium-Zinc Oxide for Buffer Layer Free Semitransparent Perovskite Photovoltaic Devices in Perovskite/Silicon 4T-Tandem Solar Cells. *Adv. Mater. Interfaces* 2001604 (2020).

55 Ma, R. *et al.* Adding a Third Component with Reduced Miscibility and Higher LUMO Level Enables Efficient Ternary Organic Solar Cells. *ACS Energy Lett.* **5**, 2711-2720 (2020).

56 Chen, W. *et al.* Interfacial stabilization for inverted perovskite solar cells with long-term stability. *Sci. Bull.* **66**, 991-1002 (2021).

57 Tan, H. Q., Zhao, X., Birgersson, E., Lin, F. & Xue, H. Optoelectronic modeling and sensitivity analysis of a four-terminal all-perovskite tandem solar cell – Identifying pathways to improve efficiency. *Sol. Energy* **216**, 589-600 (2021).

58 Xue, H., Fu, K., Wong, L. H., Birgersson, E. & Stangl, R. Modelling and loss analysis of meso-structured perovskite solar cells. *J. Appl. Phys.* **122**, 083105 (2017).

59 Zhang, T. *et al.* Analysis of a device model for organic pseudo-bilayer solar cells. *J. Appl. Phys.* **112**, 084511 (2012).

60 Hurkx, G. A. M., Klaassen, D. B. M. & Knuvers, M. P. G. A new recombination model for device simulation including tunneling. *IEEE. T. Electron Dev.* **39**, 331-338 (1992).

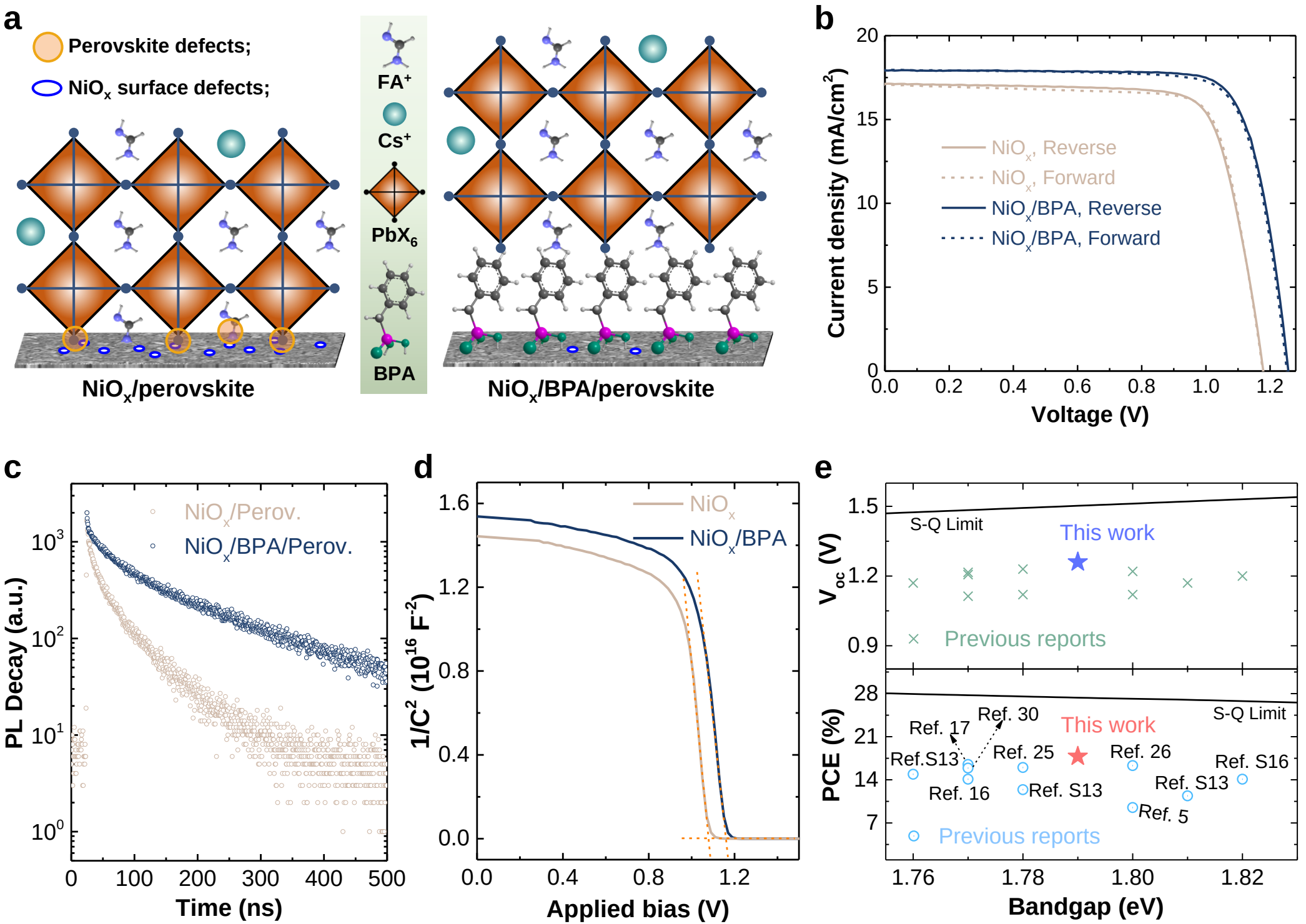
a
Perovskite defects;
NiOx surface defects;
FA+
Cs+
PbX6
BPA
NiOx/perovskite
NiOx/BPA/perovskite
b
Current density (mA/cm2)
Voltage (V)
NiOx, Reverse
NiOx, Forward
NiOx/BPA, Reverse
NiOx/BPA, Forward
c
PL Decay (a.u.)
Time (ns)
NiOx/Perov.
NiOx/BPA/Perov.
d
1/C2 (10^16 F-2)
Applied bias (V)
NiOx
NiOx/BPA
e
Voc (V)
S-Q Limit
This work
Previous reports
PCE (%)
Bandgap (eV)
Ref. 17
Ref. 30
Ref.S13
Ref. 25
Ref. 26
Ref. S16
Ref. 16
Ref. S13
Ref. S13
Ref. 5

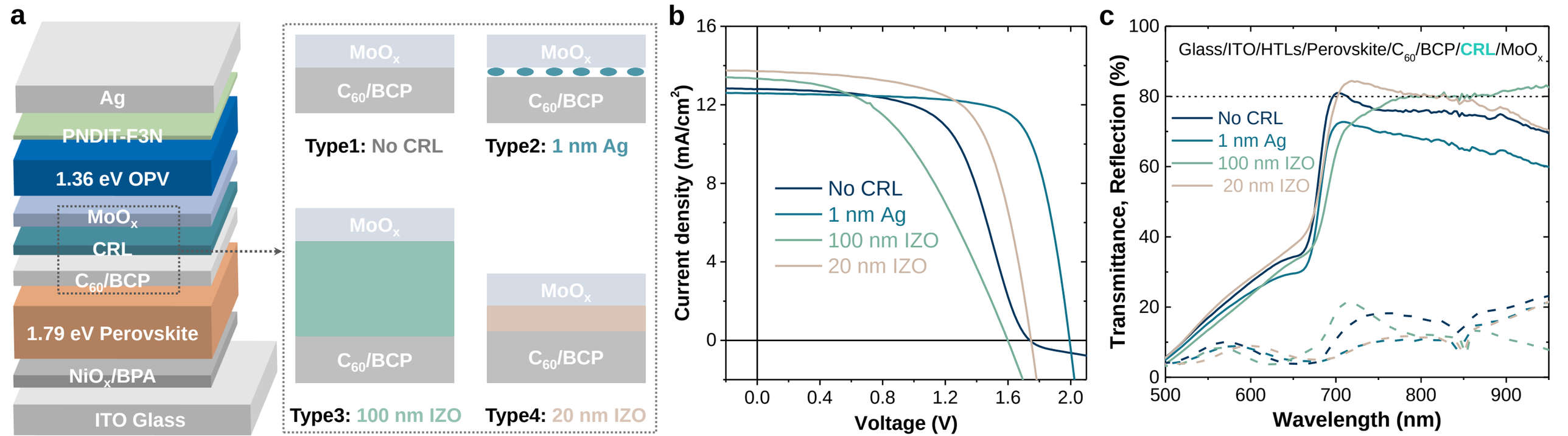
a
Ag
PNDIT-F3N
1.36 eV OPV
MoOx
CRL
C60/BCP
1.79 eV Perovskite
NiOx/BPA
ITO Glass
MoOx
C60/BCP
Type1: No CRL
MoOx
C60/BCP
Type2: 1 nm Ag
MoOx
C60/BCP
Type3: 100 nm IZO
MoOx
C60/BCP
Type4: 20 nm IZO
b
Current density (mA/cm2)
Voltage (V)
No CRL
1 nm Ag
100 nm IZO
20 nm IZO
c
Glass/ITO/HTLs/Perovskite/C60/BCP/CRL/MoOx
Transmittance, Reflection (%)
Wavelength (nm)
No CRL
1 nm Ag
100 nm IZO
20 nm IZO

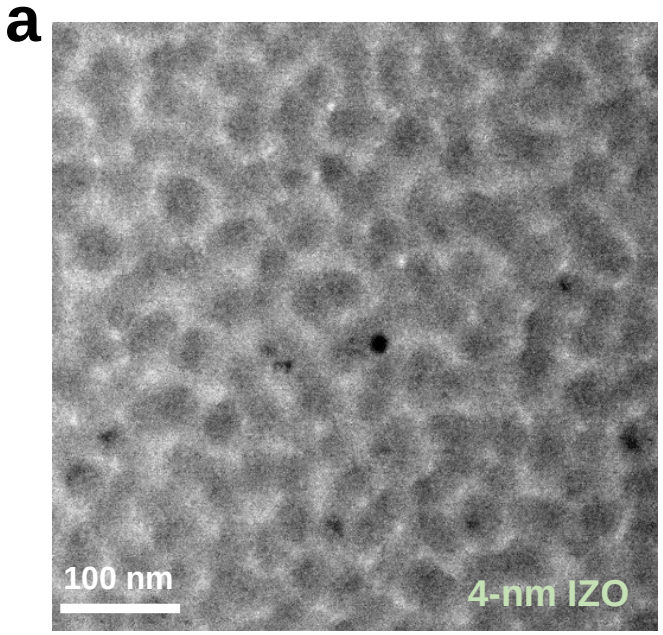
a
100 nm
4-nm IZO

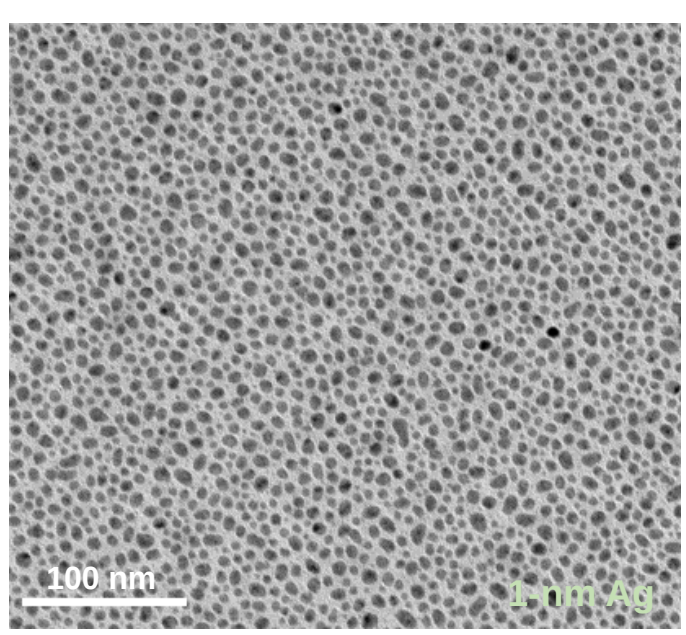
b
100 nm
1-nm Ag

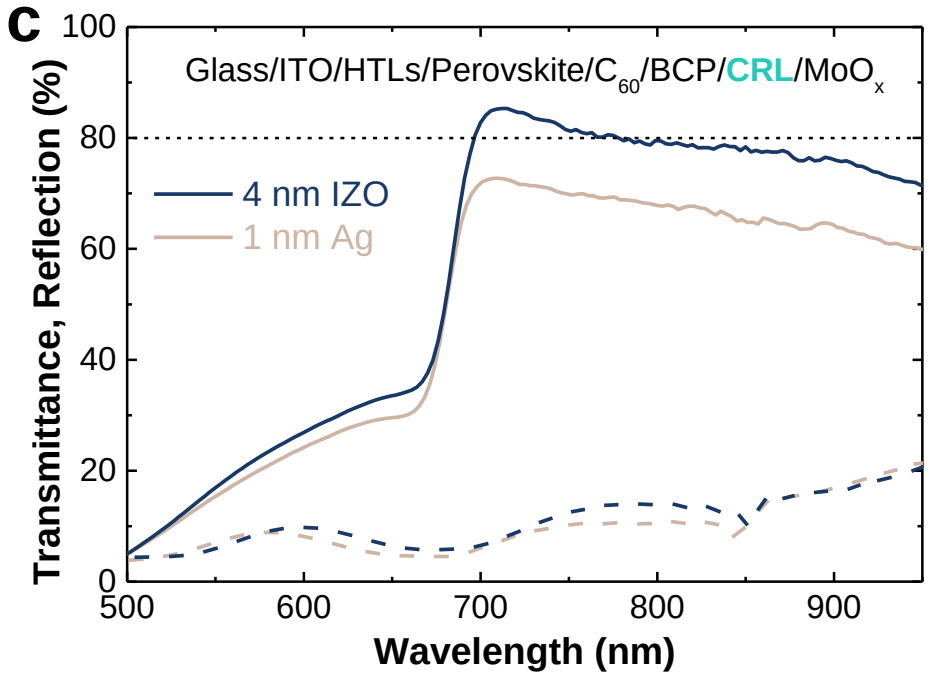
c
Glass/ITO/HTLs/Perovskite/C60/BCP/CRL/MoOx
4 nm IZO
1 nm Ag
Transmittance, Reflection (%)
Wavelength (nm)

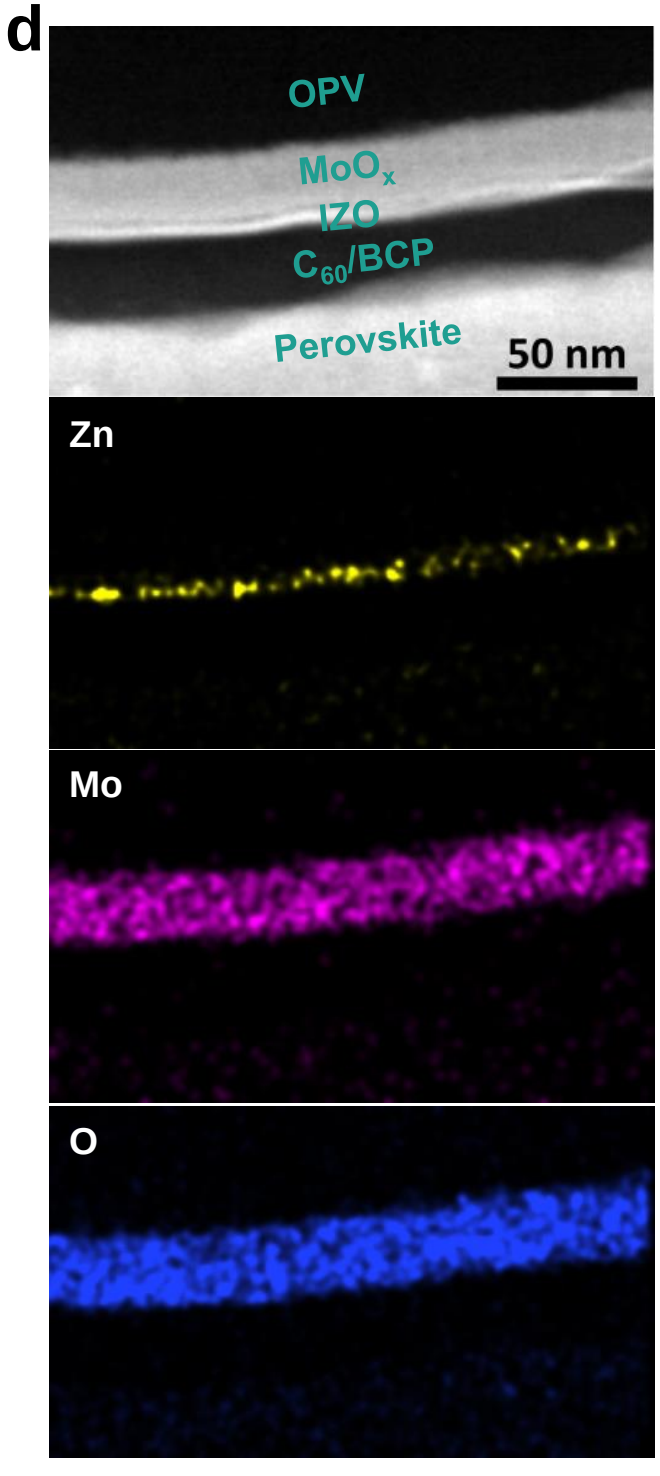
d
OPV
MoOx
IZO
C60/BCP
Perovskite
50 nm
Zn
Mo
O

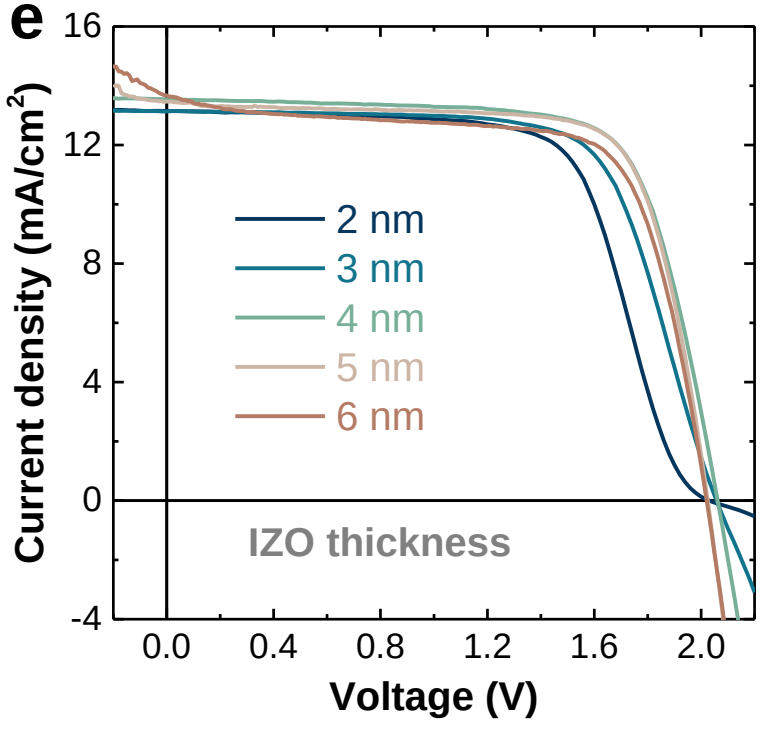
e
2 nm
3 nm
4 nm
5 nm
6 nm
IZO thickness
Current density (mA/cm2)
Voltage (V)

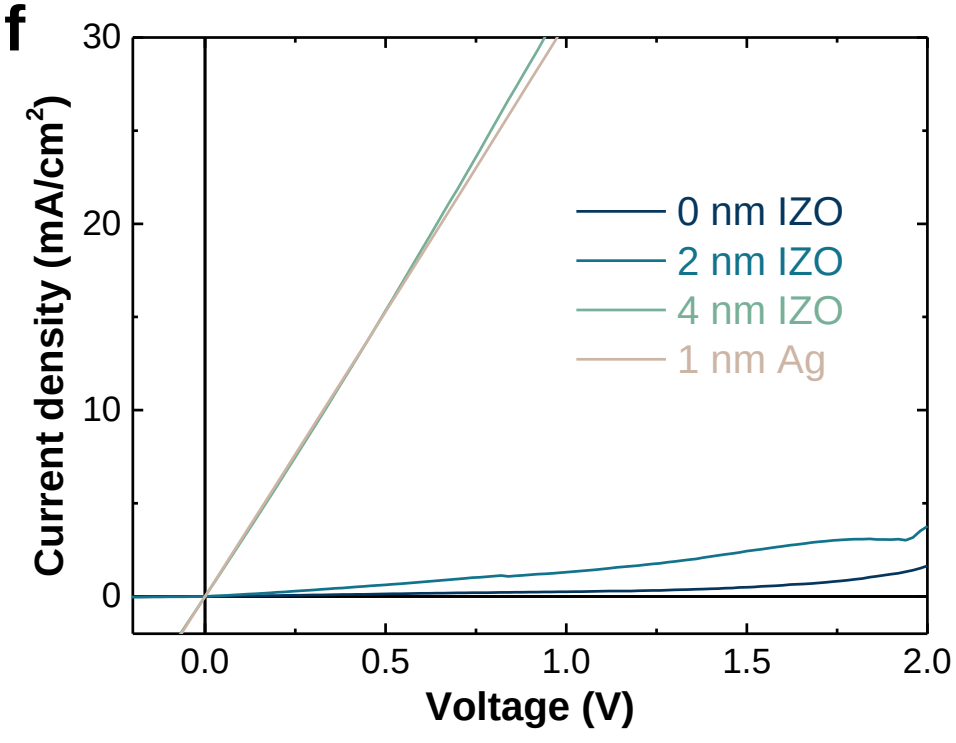
f
0 nm IZO
2 nm IZO
4 nm IZO
1 nm Ag
Current density (mA/cm2)
Voltage (V)

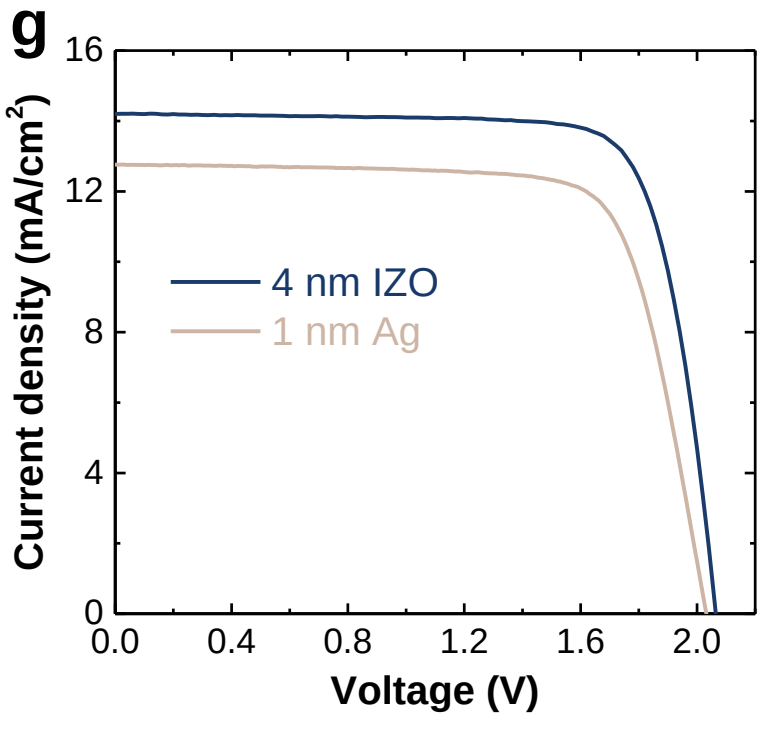
g
4 nm IZO
1 nm Ag
Current density (mA/cm2)
Voltage (V)

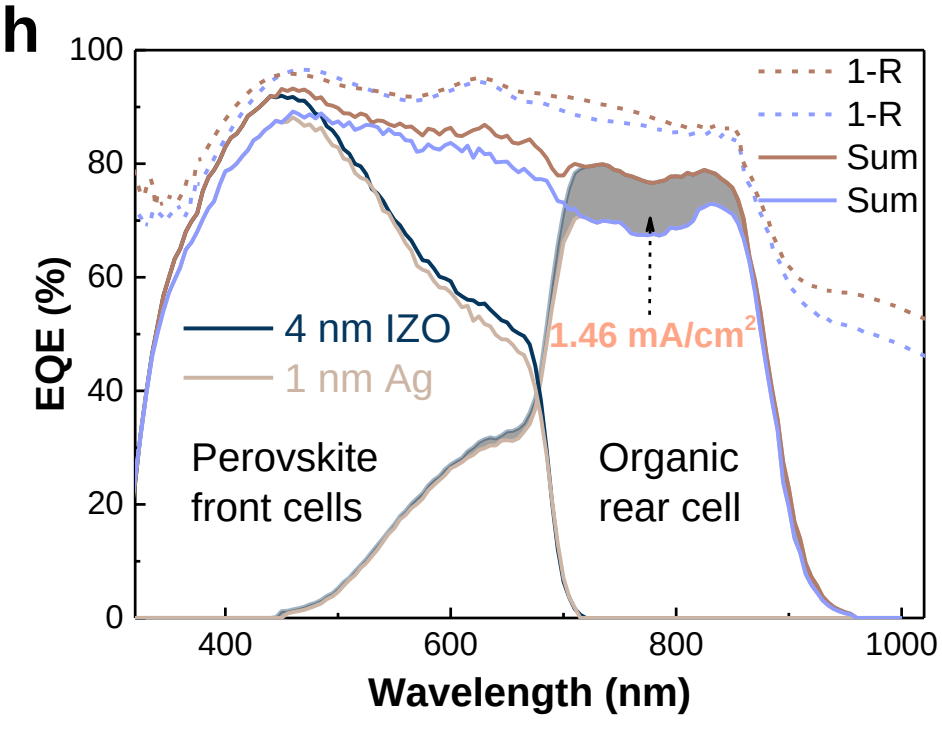
h
1-R
1-R
Sum
Sum
4 nm IZO
1 nm Ag
1.46 mA/cm2
Perovskite
front cells
Organic
rear cell
EQE (%)
Wavelength (nm)

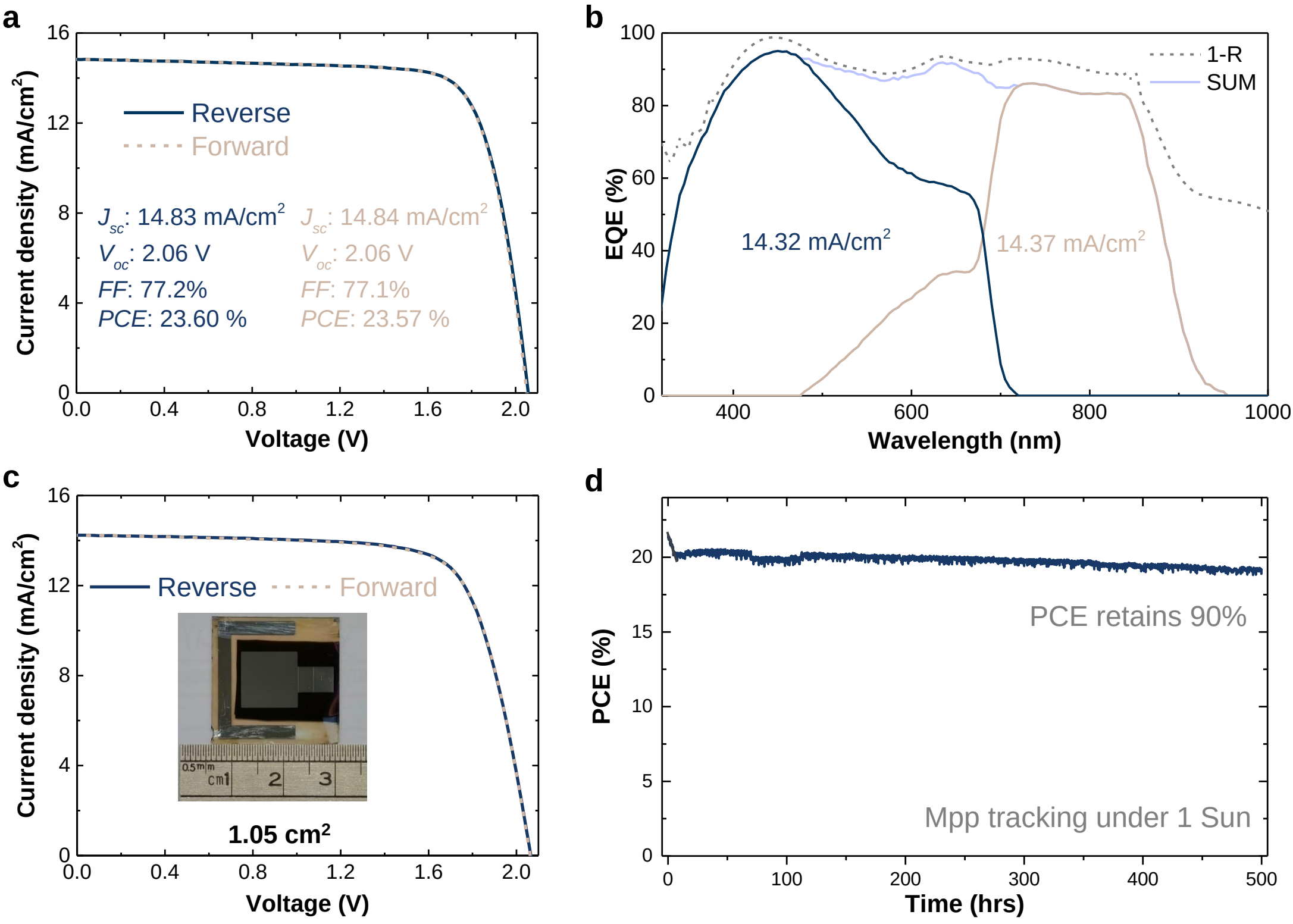
a
Current density (mA/cm²)
Voltage (V)
Reverse
Forward
Jsc: 14.83 mA/cm²
Voc: 2.06 V
FF: 77.2%
PCE: 23.60 %
Jsc: 14.84 mA/cm²
Voc: 2.06 V
FF: 77.1%
PCE: 23.57 %
b
EQE (%)
Wavelength (nm)
1-R
SUM
14.32 mA/cm²
14.37 mA/cm²
c
Current density (mA/cm²)
Voltage (V)
Reverse
Forward
1.05 cm²
d
PCE (%)
Time (hrs)
PCE retains 90%
Mpp tracking under 1 Sun